LRP 475/93 June 1993

Papers contributed to the
20th EPS CONFERENCE ON CONTROLLED
FUSION AND PLASMA PHYSICS

Lisboa, Portugal
July 26 - 30, 1993

LIST OF CONTENTS

# BETA LIMITS FOR TOKAMAKS WITH A LARGE BOOTSTRAP FRACTION

A. Bondeson
Centre de Recherches en Physique des Plasmas, Association Euratom -Confédération Suisse,
Ecole Polytechnique Fédérale de Lausanne, Lausanne/Switzerland

**I. INTRODUCTION.** There is currently a strong interest in the possibility of operating a tokamak in steady state with the major part of the current coming from the bootstrap effect, supplemented by some "seed" current in the central region, e.g., from radio frequency current drive. There are several open questions concerning such bootstrapped tokamaks, e.g., the beta limits and the amount of current drive required. The bootstrap current tends to broaden the current profile, which typically has detrimental effects on the confinement time and beta limit [1]. A theoretical estimate for the beta limit of a bootstrapped tokamak limit was given in [2]. It was shown to scale as $\varepsilon^{1/2} g^2 c_{bs} (1+\kappa^2)$, where $g = \beta/I_N$ is the Troyon coefficient, $I_N = I[MA]/(a[m]B_0[T])$ the normalized plasma current, $\kappa$ is the elongation and $c_{bs}$ quantifies the efficiency of the bootstrap current generation. Although analytical estimates can be given for $c_{bs}$, and the behavior of g is quite well known, a realistic assessment of the bootstrapped tokamak requires quantitative knowledge of what values of g and $c_{bs}$ can be obtained when the current and pressure profiles are related by the bootstrap mechanism. Here, we address this question by global numerical calculations and compute beta limits for bootstrapped tokamaks with differently shaped cross section. The main result is that this beta limit is highly sensitive to shaping and increases with elongation and triangularity.

**II. PROFILE EFFECTS.** In tokamaks operated at high current, the beta limit generally increases with the internal inductance; $g \leq 4l_i$ is reported from DIII-D [1]. This is characteristic of the "first stability" regime of high-n ballooning modes. The pressure profiles that are optimal for MHD stability are rather broad with peaking factors (PPF = $p_0/\langle p\rangle$) typically around 2. (Experimentally, the highest beta values tend to occur for more peaked pressure profiles, which may be in the second stability regime in the central region due to negative shear [3]). At high poloidal beta, the bootstrap mechanism broadens the current distribution, which is destabilizing for the n = 1 free boundary kink mode. On the other hand, for current profiles with low shear in the central region, the high-n ballooning modes can enter into the "second stability" region. This transition is favoured by D-shaping and high q. The possibility that also the external kink mode of toroidal mode number n = 1 could reach second stability was suggested in [4]. Figure 1 shows the results of an attempt to test this, using the ERATO stability code. The figure shows g-factors vs. internal inductance for the free boundary stability of strongly D-shaped equilibria with broad current profiles, $0.5 < l_i < 0.8$ and $1.8 < q_0 < 5$ and peaked pressure profiles, $3 \leq PPF \leq 4$. In this paper, we use the following definitions for beta, poloidal beta and internal inductance

$$\beta = \frac{2\mu_0\langle p\rangle}{\langle B^2\rangle} \quad , \qquad \beta_p = \frac{2\mu_0\langle p\rangle}{\langle B_p\rangle_s^2} \quad , \qquad l_i = \frac{\langle B_p^2\rangle}{\langle B_p\rangle_s^2} \quad , \qquad (1)$$

where $\langle\bullet\rangle$ means volume average and $\langle B_p\rangle_s = \mu_0 I_p / L$, with L the plasma circumference, denotes the line average on the surface. The moderate g-factors in Fig. 1 show that the free boundary n = 1 mode does not reach second stability for equilibria of this type, even for very

high $q_0$. Nevertheless, Fig. 1 shows some reminiscences of second stability, e.g., g increases with decreasing inductance when the pressure profile is peaked. Thus, for highly shaped equilibria with peaked pressure and broad current profiles, the $l_i$-dependence is opposite to that found in the standard regime of high inductance and broad pressure profiles. When the data points in Fig. 1 are plotted vs. the pressure peaking factor we find that for PPF > 3, the g-factors decrease strongly when the pressure is further peaked.

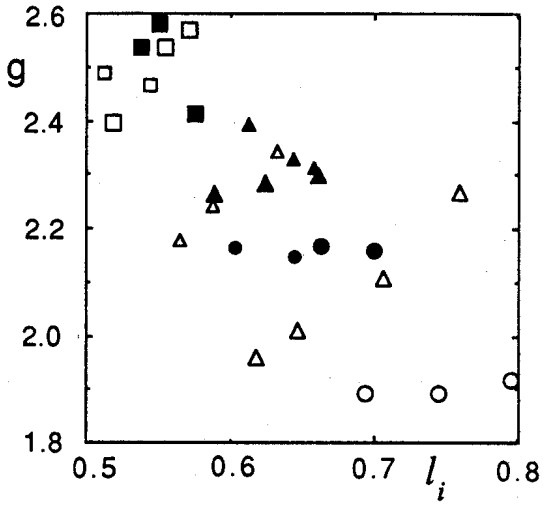


*FIGURE 1. g-factors vs. $l_i$ for peaked pressure profiles and A = 3, κ = 2.5, δ = 0.6.*

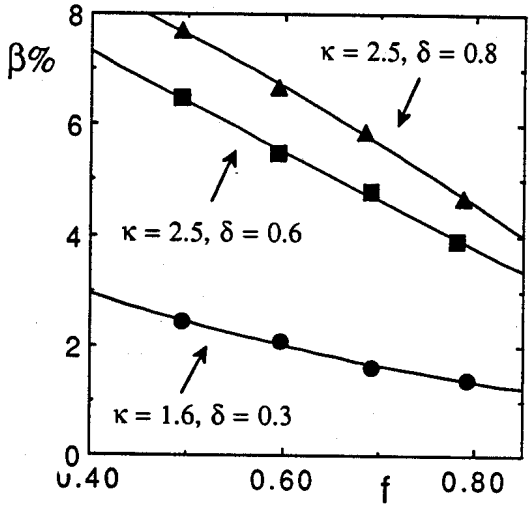


*FIGURE 2. Optimized β vs. bootstrap fraction f for different cross sections.*

**III. NUMERICAL RESULTS.** A beta-limit study for bootstrapped tokamaks has been carried out with a partial optimization of the profiles. Profiles are specified for the surface averaged toroidal current density $I^*(\psi) = \langle j_\phi/R \rangle$. Then, the pressure profile is chosen so that the parallel bootstrap current [computed from the formulas of Hirshman [5] with $T_e = T_i = T$, Z = 1, and $\eta = d(\log T)/d(\log n) = 1.5$] is a fixed fraction of the total parallel current for all $\psi$, except in the center where a cut-off has been applied to $dp/d\psi$. The resulting pressure peaking factor is generally between 2.5 and 3. The total bootstrap current is computed as

$$I_{bs} = \int_{\phi = \text{const}} \frac{\langle j_{bs} \cdot B \rangle}{\langle j \cdot B \rangle} \, j_\phi \, dS \quad . \qquad (2)$$

The current profile has been varied over a restricted set with $I^* = 0$ at the edge to find an optimum for the beta limit. With the pressure and current profiles related so that the bootstrap fraction is (almost) independent of $\psi$, the optimal current profiles are broad, in particular, for strongly shaped cross sections. It appears that the geometrical effects of shaped cross sections on the q-profile favour broader current profiles, and this is advantageous for the bootstrapped tokamak. The numerical results are shown in Fig. 2 as $\beta_{max}$ vs. the bootstrap fraction $f = I_{bs}/I_p$. The curves represent three different cross sections, one JET-like with elongation κ = 1.6 and triangularity δ = 0.3 and two DIII-D-like (κ = 2.5 and two triangularities δ = 0.6 and 0.8) all at aspect ratio 3. The figure shows that D-shaping has a clearly favorable effect. The results indicate that operation with a high bootstrap fraction should be of interest in strongly shaped machines such as DIII-D and TCV, while this scenario gives very low beta limits in weakly shaped machines such as JET.

**IV. THEORY.** Analytical arguments [2] can be applied to the numerical results to understand the dependence on shaping. The equilibria can be characterized by two figures of merit which determine the beta limit of the bootstrapped tokamak. These are the Troyon coefficient $g = \beta[\%] / I_N$ and the bootstrap factor $c_{bs}$, defined by writing the bootstrap fraction as

$$f = \frac{I_{bs}}{I_p} = c_{bs}\, \varepsilon^{1/2}\, \beta_p \quad . \tag{3}$$

The definition (3) is motivated by the following considerations. To lowest order in inverse aspect ratio, the bootstrap current density is

$$j_{bs} \approx c\, \varepsilon(\psi)^{1/2}\, R_0\, (dp/d\psi) \quad , \tag{4a}$$

where $c = [2.44(T_e+T_i)n' + n(0.69T_e'-0.42T_i')]/p$. In the numerical examples, $T_e = T_i$ and $\eta = 1.5$, so that $c \approx 0.9$. Assuming a flat q-profile and parabolic pressure profile, the total bootstrap current can be integrated to give $I_{bs} = 3.2\pi\, c\, \varepsilon^{1/2}\, R_0 q \langle p \rangle / B_0$, which may be rewritten as

$$I_{bs,N} = \frac{I_{bs}[MA]}{a[m]B_0[T]} = 0.2c\, \varepsilon^{1/2}\, \frac{qI_N}{5\varepsilon}\, \frac{\beta[\%]}{I_N} \quad . \tag{4b}$$

Furthermore, the definitions (1) imply $\beta_p = (\beta[\%]/4I_N^2)\, (L/2\pi a)^2$, thus (4b) gives (3) with $c_{bs} = 0.8c\, (qI_N/5\varepsilon)\, (2\pi a/L)^2$. In the case of an elliptical cross section and q = constant, the geometrical factors in $c_{bs}$ almost cancel because $qI_N/5\varepsilon = (1+\kappa^2)/2 \approx (L/2\pi a)^2$. Consequently, $c_{bs}$ should be independent of ellipticity and approximately equal to 0.8c. Of course, in general, $c_{bs}$ also depends on the pressure and current profiles. Taking the square of the Troyon law the beta limit can be expressed as $\beta[\%]\beta_p < (g_{max}^2/4)\, (L/2\pi a)^2$. In combination with (3), this gives the following beta limit for the bootstrapped tokamak

$$\beta[\%] < \varepsilon^{1/2}\, g_{max}^2\, (c_{bs}/4f)\, (L/2\pi a)^2. \tag{5}$$

It also follows that there is a limit to the bootstrap current set by MHD stability

$$I_{bs,N} < \varepsilon^{1/2}\, g_{max}\, (c_{bs}/4)\, (L/2\pi a)^2. \tag{6}$$

For weakly shaped cross sections, Eq. (6) gives rather low values of the bootstrap current. Examination of the numerical results in Fig. 2 shows that for each geometry and self-similar sequence of I*-profiles, $g_{max}$ and $c_{bs}$ are approximately constant for bootstrap fractions f between 50 % and 70 %. Thus, the 1/f scaling for the beta limit in (5) holds quite well and the results can be summarized by giving $g_{max}$ and $c_{bs}$. These are quoted together with $\beta$ at 70 % bootstrap fraction, $l_i$ and $I_{bs,N}$ in Table I for equilibria of different cross sections, with profiles optimized as described in Sec. II. Table I underlines the favorable effect of shaping on the beta limit of bootstrapped tokamaks. Note that even modest variations of g affect $\beta$ significantly because g is squared in (5). It appears that g is slightly reduced by ellipticity but increased by triangularity. For the bootstrapped current profiles with $\langle \mathbf{j}_{bs} \cdot \mathbf{B} \rangle \approx f \langle \mathbf{j} \cdot \mathbf{B} \rangle$, g reaches the highest values for rather low $l_i$ . The optimal current profiles are flatter the more shaped the cross section is, as seen from the values of $l_i$ in Table I. Furthermore, g decreases if the pressure profile becomes too peaked, say PPF > 3.

| $\kappa$ | $\delta$ | $c_{bs}$ | g | $\beta$ [%] | $I_{bs,N}$ | $l_i$ |
|---|---|---|---|---|---|---|
| 1.6 | 0.3 | 0.82 | 2.23 | 1.6 | 0.50 | 0.72 |
| 2.0 | 0.5 | 0.82 | 2.63 | 3.2 | 0.84 | 0.64 |
| 2.5 | 0.6 | 0.83 | 2.68 | 4.7 | 1.24 | 0.56 |
| 2.5 | 0.8 | 0.80 | 3.06 | 6.2 | 1.39 | 0.56 |

*TABLE I. Characteristics of beta-optimized equilibria with 70 % bootstrap current in different geometries at aspect ratio 3.*

The bootstrap coefficient $c_{bs}$ is insensitive to the equilibrium profiles, although broad profiles give somewhat higher values because of the $\varepsilon^{1/2}/B_p$ weighting in (4a). As seen from Table I, $c_{bs}$ is also almost independent of the shape of the cross section and is close to the simple analytical estimate 0.8. ($c_{bs}$ increases somewhat with the peaking of the density relative to the temperature, which has been held fixed in this study, although this dependence is weaker at low aspect ratio.) The profiles of pressure and parallel current $\langle j_{bs} \cdot B \rangle$ and $\langle j \cdot B \rangle$ for the case $\kappa = 2.5$, $\delta = 0.6$ (with 70 % bootstrap current and $\beta = 4.7$ %) are shown vs. $s = \psi^{1/2}$ in Fig. 3. The current profile is nonstandard and very broad. It is clear that this type of profile may be difficult to maintain and control in steady state.

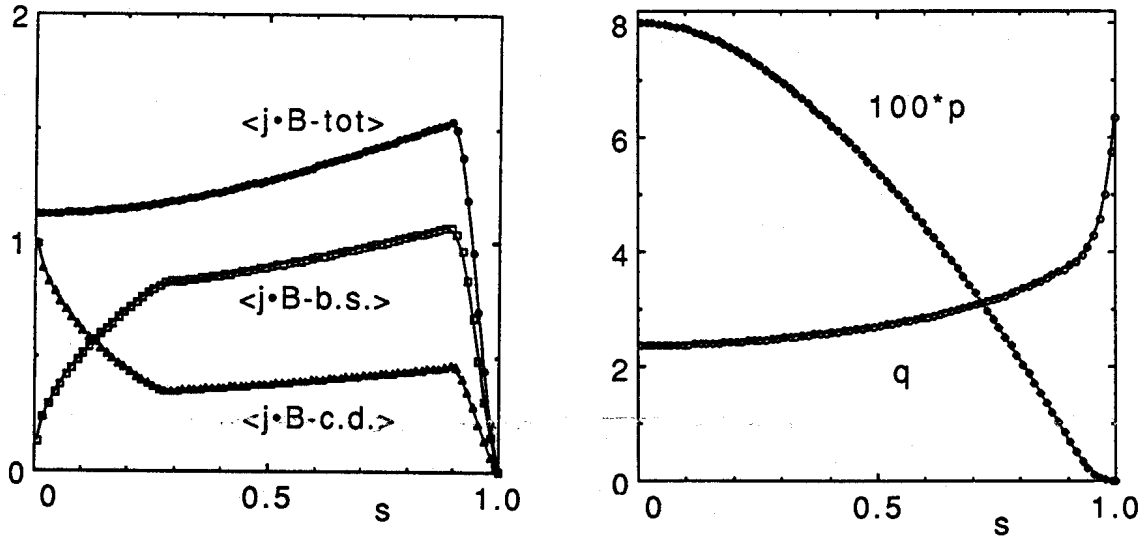


*FIGURE 3. Profiles of parallel current $\langle j \cdot B \rangle$, pressure and q vs. $s = \psi^{1/2}$ for an equilibrium with 70 % bootstrap current, $\beta = 4.7$ %, $\kappa = 2.5$, $\delta = 0.6$ and A = 3 (see Table I).*

## REFERENCES

[1] T.S. Taylor, et al., Proc. 13th IAEA Conf., Wash., D.C., 1990, Vol. 1, p. 177.
[2] R.H. Weening and A. Bondeson, Comm. Plasma Phys. Contr. Fusion **15**, 77 (1992).
[3] E.A. Lazarus, et al, Phys. Fluids **B4**, 3644 (1992).
[4] J.J. Ramos, Phys. Fluids **B3**, 2247 (1991).
[5] S.P. Hirshman, Phys. Fluids **31**, 3150 (1988).

# IDEAS IN TOKAMAK CONCEPT IMPROVEMENT

W. A. Cooper and F. Troyon
Centre de Recherches en Physique des Plasmas,
Association Euratom-Confédération Suisse,
Ecole Polytechnique Fédérale de Lausanne,
Lausanne, Switzerland

It is experimentally observed that the transport properties of tokamak devices improve with the transformer-induced toroidal plasma current. For configurations in the parameter range of the ITER (International Tokamak Experimental Reactor) device, however, the toroidal current requirements predicted become very large ( $25MA$). Steady state operation is impossible and disruption phenomena triggered by these currents could cause severe damage to the vacuum vessel and other systems of the device. It would be thus of great interest to devise a way to relax the toroidal currents needs without degrading the confinement properties. One possible approach that we propose here is the use of external helical windings to sustain a significant fraction of the edge rotational transform. The tokamak, however, ceases to be axisymmetric and becomes a three-dimensional (3D) configuration.

We consider here a circular cross section tokamak with finite toroidal current on which we impose a $L = 3$ external helical field to produce a triangular deformation of the plasma that rotates toroidally. The application of $L = 1$ or $L = 2$ components, or combinations thereof could also be considered. But we have decided to limit the scope of the study so far to $L = 3$ components motivated by the fact that this class of field only alters the external region of the plasma. The bulk of the plasma where the pressure concentrates remains essentially a conventional tokamak. The basic configuration has 8 periods and an aspect ratio $A = 10$, large enough to permit comparisons with analytic calculations. The plasma boundary is prescribed as

$$R = R_{00}(1) + R_{10}(1)cosu + \delta cos(u - Nv) + \delta cos(u - 3Nv), \quad (1)$$
$$Z = R_{10}(1)sinu + \delta sin(u - Nv) - \delta sin(u - 3Nv), \quad (2)$$

where $R_{00}(1) = 10$, $R_{10}(1) = 1$, $\delta = -0.055$ and $N = 8$. We use the VMEC equilibrium code [1] to compute 3D equilibria that selfconsistently model tokamaks with externally applied helical fields. This code imposes nested magnetic flux surfaces on the configurations investigated. The coordinate system is $(s, u, v)$ where $0 \leq s \leq 1$ is the radial variable, $0 \leq u \leq 2\pi$ is the poloidal angle and $0 \leq v \leq 2\pi/N$ is the toroidal angle. The magnetic axis is at $s = 0$ and the plasma boundary is at $s = 1$. In order to calculate 3D tokamak equilibria, we must prescribe two surface functions. One is the pressure profile given by

$$p(s) = p(0)(1 - s - 0.5s^2 + 0.5s^4). \quad (3)$$

This choice makes the pressure gradients relatively weak in the outer region dominated by the stellarator fields. The toroidal plasma current enclosed within each flux surface

$s$ is prescribed as

$$2\pi J(s) = \frac{8}{15}[2\pi J(0)]\Big(s - \frac{2}{3}s^3 + \frac{1}{5}s^5\Big). \tag{4}$$

The normalised toroidal current shown in the results is defined as $J(1)R_{10}(1)/\Phi(1)$, where $2\pi\Phi$ is the toroidal magnetic flux. The rotational transform profiles for a tokamak at $\beta^* = 1.55\%$ and normalised toroidal current equal to 0.0433 are shown for a case of an external $L = 3$ helical field ($\delta = -0.055$) and for the axisymmetric case ($\delta = 0$) in Fig. 1. This example illustrates the point that the bulk plasma is basically a conventional tokamak, while the stellarator fields provide the rotational transform support in the near force-free plasma edge. We define $\beta^* = (V \int d^3x p^2)^{1/2} / \int d^3x (B^2/2)$, where V is the plasma volume.

The TERPSICHORE package of codes [2] has been employed to investigate the Mercier, the ballooning and the global external ideal magnetohydrodynamic (MHD) stability properties of the 3D tokamaks under consideration. Within the parameter ranges that we have explored, the ballooning modes yield more restrictive criteria on local stability than the Mercier modes. The stability calculations are performed in the Boozer magnetic coordinate system [3] and the parallel current density is calculated to consistently satisfy the condition of charge conservation [4]. For the ballooning calculations, the spectrum of modes in the Boozer coordinate system includes poloidal mode numbers $m$ upto 60. Nevertheless, we find that this is insufficient to correctly converge ballooning eigenstructures in the outer edge of the plasma where the stellarator fields dominate when the Shafranov shift approaches and exceeds 50% of the minor radius for cases with $\beta^* > 1.5\%$. Upto 84 mode pairs are employed to determine the stability to $n = 1$ modes. An axisymmetric conducting wall is placed at 3 times the average minor radius to simulate a wall at infinity. We find that for the configuration examined, the coupling between different toroidal modes within the $n = 1$ family [2] is weak. The calculations are performed on 48, 56, 68 and 96 radial intervals within the plasma. The number of interval in the vacuum region corresponds to 1/4 that within the plasma. The convergence is quadratic in the mesh size. In Fig. 2, we show the converged eigenvalue for $n = 1$ external modes as a function of the normalised toroidal current. Each curve corresponds to different values of the parameter $\beta^*$, ranging from 0.99% to 3.22%. The stability results we have obtained are summarised in Fig. 3. The dotted curve in the figure constitutes the Shafranov shift equal to half the minor radius in the normalised toroidal current and $\beta^*$ parameter space. The domain above this curve corresponds to Shafranov shifts that are smaller and that below to shifts that are larger. Two regions of stable ballooning operation are obtained. In the high current region, the ballooning stability limits improve with increasing current This property characterises typical operation in the first stability regime of a conventional tokamak. The region is limited from above in the figure by the emergence of the $q = 1$ surface from the magnetic axis. In the lower current ballooning stable region, we find that for fixed $\beta^*$, the stability properties improve with decreasing plasma current. This would characterise operation in a second stable regime. However, as the current decreases, the Shafranov shift becomes increasingly large, leading eventually to convergence difficulties in the equilibrium and stability computations. The external $n = 1$ global ideal modes yield a more restrictive limit than the ballooning modes, as shown by the solid curve in Fig. 3. For $\beta^* > 1.5\%$, the limit imposed by the external modes is closely aligned with

a Shafranov shift of half the minor radius. The stable domain lies below the curve. One important difference with the conventional tokamak second stability operation is that a second stable window for the $n = 1$ modes is demonstrated here with a wall far from the plasma [5].

In conclusion, we have investigated the ideal MHD stability limits of a tokamak device of aspect ratio 10 and circular cross section on which we have superimposed a $L = 3$ external helical field to reduce the plasma current required to sustain the rotational transform at the edge of the plasma at finite $\beta$. We have demonstrated that the helical fields and the plasma current combine to permit access to the tokamak second stable regime, where not only the ballooning modes but also the $n = 1$ external modes are stabilised. For values of $\beta^* > 1.5\%$, the limit imposed by the $n = 1$ modes almost coincides with a Shafranov shift of half the minor radius.

**REFERENCES**


[1] S. P. Hirshman and O. Betancourt, *J. Comput. Phys.* **96** (1991) 99.

[2] D. V. Anderson, W. A. Cooper, R. Gruber, S. Merazzi and U. Schwenn, *Int. J. Supercomp. Appl.* **4** (1990) 34; W. A. Cooper, G. Y. Fu R. Gruber, S. Merazzi, U. Schwenn, D. V. Anderson, *Proc. Joint Varenna – Lausanne Int. Workshop on Theory of Fusion Plasmas* (Editrice Compositori, Bologna) (1990) 655.

[3] A. H. Boozer, *Physics Fluids* **23** (1980) 904.

[4] J. Nührenberg, R. Zille, *Proc. Joint Varenna – Lausanne Int. Workshop on Theory of Fusion Plasmas* (Editrice Compositori, Bologna) (1988) 3.

[5] S. C. Jardin, A. Bhattacharjee, A. Bondeson, M. S. Chance, S. C. Cowley et al., *Proc. 14th Int. Conf. Plasma Phys. Contr. Nucl. Fusion* IAEA-CN-56/D-4-13, Würzburg, FRG 1992.


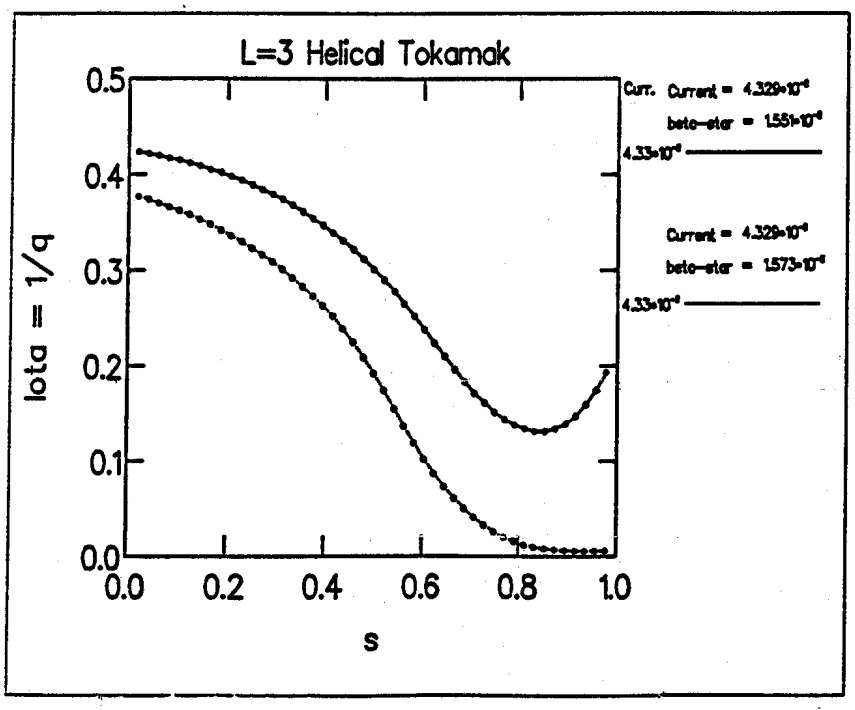


Figure 1: The rotational transform profiles in tokamaks with external $L = 3$ helical windings (upper curve, $\delta = -0.055$) and without them (lower curve, $\delta = 0$). The normalised toroidal current is 0.0433 and $\beta^* = 1.55\%$ in both cases.

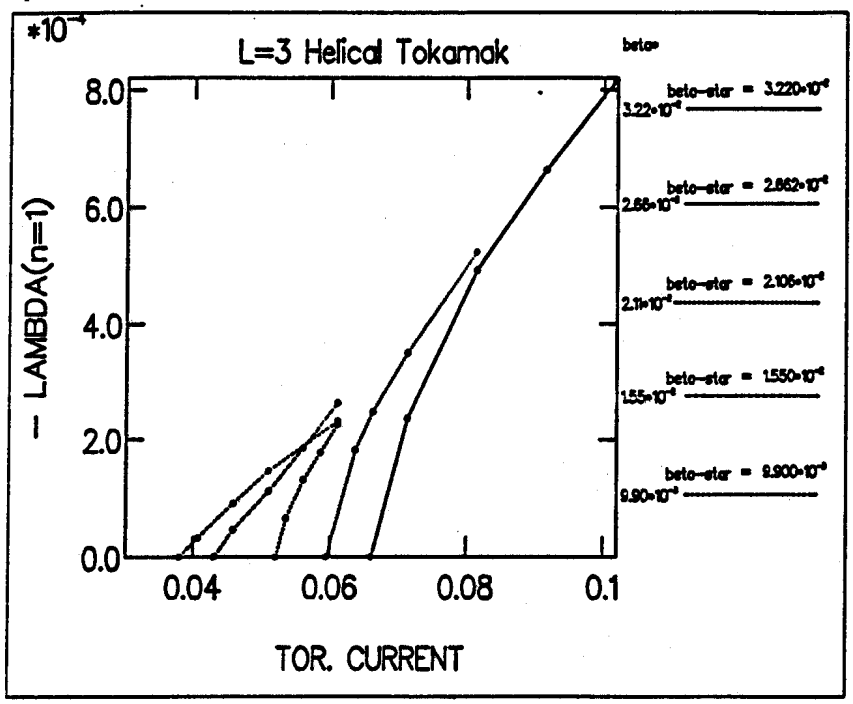


Figure 2: The converged eigenvalue of external $n = 1$ modes with conducting wall at infinity for a tokamak with $L = 3$ helical windings as a function of the normalised toroidal current. The curves correspond to values of the parameter $\beta^*$ of 0.99%, 1.55%, 2.106%, 2.662% and 3.22% from low current to high current.

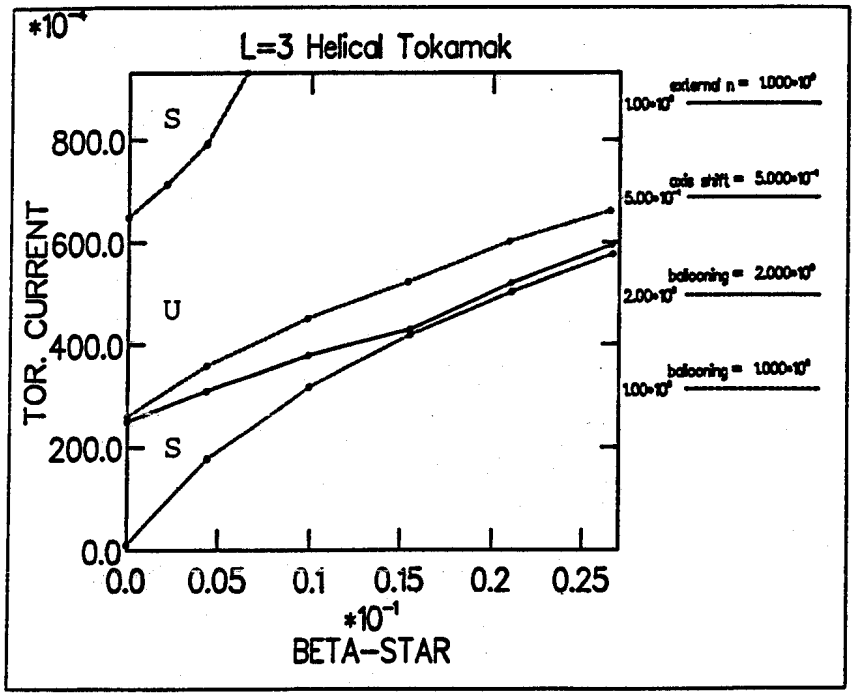


Figure 3: The stability boundaries in a tokamak with external $L = 3$ helical fields in the parameter space of normalised toroidal current versus $\beta^*$. The dashed curve that bounds the upper left hand corner constitutes the first ballooning stable domain. The region below the other dashed curve constitutes the second ballooning stable domain. The region below the solid curve is stable to $n = 1$ external modes. The domain above the dotted curve has a Shafranov shift smaller than half the minor radius.

# MHD EQUILIBRIUM AND STABILITY OF DOUBLET CONFIGURATIONS

S. Medvedev*, L. Villard, L.M. Degtyarev*, A. Martynov*, R. Gruber** and F. Troyon

Centre de Recherches en Physique des Plasmas
Association EURATOM - Confédération Suisse,
Ecole Polytechnique Fédérale de Lausanne
21, Av. des Bains, CH-1007 Lausanne, Switzerland

* Keldysh Institute of Applied Mathematics, Russian Academy of Sciences, Miusskaya sq. 4, Moscow 135047, Russia

** R. Gruber, Gruppo Applicazione Scientifiche della Svizzera, Centro Svizzero di Calcolo Scientifico, Via Cantonale, CH-6928 Manno, Switzerland

1. The operational limits of tokamak configurations with single magnetic axis imposed by ideal MHD stability have been intensively studied in the last decade [1]. Much less efforts have been made to investigate plasmas with external separatrix [2]. On the other hand, plasmas with external separatrix are used in modern tokamaks to obtain better confinement. Doublet configurations with two magnetic axes and a separatrix inside the plasma may have different confinement properties than single axis tokamaks. Doublet tokamak configurations were tried experimentally [3] but were not studied in detail theoretically [4]. In order to determine the operational space of these configurations allowed by ideal MHD constraints, a package of equilibrium and stability codes has been developed with an appropriate treatment of the internal separatrix. Some stability results for $n = 0$ and $n = 1$ ideal MHD modes are presented.

2. The poloidal flux function $\psi(r,z)$ for an axisymmetric equilibrium magnetic field $B = \nabla\psi \times \nabla\phi + F(\psi)\nabla\phi$ satisfies the Grad-Shafranov equation:

$$\nabla \cdot \left(\frac{\nabla\psi}{r^2}\right) = -\frac{j_\phi}{r}, \qquad j_\phi = r\frac{dP}{d\psi} + \frac{1}{r}F\frac{dF}{d\psi}, \tag{1}$$

where $p(\psi)$ is the plasma pressure and $F(\psi)$ the toroidal flux function. To solve the equation one can prescribe the shape of the plasma boundary and the current density profile $j_\phi$ specifying either $dp/d\psi$ and $FdF/d\psi$ or $dp/d\psi$ and

$$I^*(\psi) = \frac{d}{d\psi}\left(\int_{S_\psi} j_\phi \, ds\right) \Big/ \frac{d}{d\psi}\left(\int_{S_\psi} ds\right) \tag{2}$$

The plasma domain is decomposed into three subdomains: two inside, and one outside the separatrix. In each subdomain a structured grid with quadrangular cells is introduced. We use a variational finite difference scheme that is the average of two finite element discretizations corresponding to two different triangularizations [5].

The mapping procedure is replaced with a grid adaptation scheme on magnetic surfaces $\psi = \text{const}$. This was already successfully used in a number of codes [5,6,7]. The iterative procedure combines grid adaptation and

Picard iterations on nonlinearity. The Grad-Shafranov equation with prescribed right-hand side is solved with an overrelaxation method. Then the hyperbolic x-point is determined and the separatrix is traced as $\psi = \psi_{x\text{-point}}$. In each of the subdomains a linear interpolation is used to match the grid points positions with magnetic surfaces. Flux functions $dp/d\psi$ and $FdF/d\psi$ or $I^*$ are then updated on the new grid and the loop is repeated.

For code verification analytical solutions were used which are superpositions of Solev'ev and vacuum solutions :

$$\begin{aligned} \psi &= \psi_0 - (r^2 - r_0^2)^2 + 4\alpha^2(r^2 - \sigma^2)z^2 \\ &+ (a + br^2)\, z + c\cos(dz)\, r\, I_1(dr), \qquad (3) \\ dp/d\psi &= 8(1 + \alpha^2), \qquad F\, dF/d\psi = -8\alpha^2\sigma^2. \end{aligned}$$

In Fig. 1 the grid adapted to magnetic surfaces is shown for $\psi_0 = 0.6$, $r_0 = 1$, $\alpha = 0.6$, $\sigma = 0.3$, $a = 0$, $b = 0.1$, $c = 0.7$, $d = 2$. The external boundary is chosen to coincide with the external separatrix.

A convergence rate $N^{-2}$(N is the number of points in one direction) is achieved for the coordinates of magnetic surfaces and those of the magnetic axes. With grid packing near the separatrix the same rate can be reached for the x-point position also.

For characteristic up-down symmetric equilibria with $N_\psi = 64$, $N_\theta = 64$, ($N_\psi$, $N_\theta$ – number of points in radial and poloidal directions) inside separatrix and $N_\psi = 32$, $N_\theta = 64$ outside, 15 iterations are needed to reach an accuracy of $10^{-5}$ in $\psi$ variations over the adapted grid. It takes 20 s on NEC SX-3/22 at 240 Mflops.

3. A variational formulation of the linearized ideal MHD equations is used for the stability code. The potential energy representation is based on the following displacement vector representation [8]:

$$\vec{\xi} = X\frac{\vec{D}\times\vec{B}}{B^2} + Y\frac{\vec{B}\times\nabla\psi}{B^2} + Z\frac{\vec{B}}{B^2}, \qquad (4)$$

where $\vec{B} = \nabla\psi \times \vec{D}$.

Flux coordinates $(\psi,\theta,\phi)$ in each subdomain and finite hybrid elements are used to avoid spectral pollution [9]. The poloidal coordinate is not fixed by a choice of the Jacobian but is defined by the equilibrium grid. Some further modifications were introduced to improve code convergence: "spectral shift" elimination [9] and numerical destabilization correction [10]. In the vacuum region between the plasma and the conducting wall a "pseudodisplacement" approach [11] is used.

Inverse iteration and a direct matrix solver are used to find the eigenvalues. The solver is based on the PAMERA code [12] modified to treat connectivity conditions between subdomains and to exploit the banded structure of matrix blocks. The connectivity conditions at the x-point are written as $X = \xi \cdot \nabla\psi = 0$.

For grid dimensions inside $N_{\psi 1} = 128$, $N_{\theta 1} = 128$, $N_{\psi 2} = 128$, $N_{\theta 2} = 128$ and outside separatrix $N_{\psi 3} = 32$, $N_{\theta 3} = 256$ the computation of one eigenvalue takes 70s at 900 Mflops on a NEC SX-3.

4. In Fig. 2 the adapted grid is shown for an up-down symmetric equilibrium with vacuum (or pressureless currentless plasma) outside

separatrix. Note that the angle between separatrix branches is $\pi/2$ at the x-point. Stability of n = 0 and n = 1 external modes was computed for such type of equilibria. For n = 0 two unstable modes are present when the conducting wall is far from the plasma. The most unstable mode corresponds to displacements of upper and lower parts of the plasma in opposite directions (Fig. 3a). The mode with lower increment corresponds to mainly vertical displacement of the whole plasma (Fig. 3b). The distance wall-plasma boundary needed to stabilize n = 0 modes is about equal to the plasma minor radius for a wall shape similar to the external boundary. This distance is close to the value needed to stabilize a single axis plasma inside the separatrix taken alone (the elongation is 1.5 for the case considered).

Limiting $\beta$-values against n = 1 external mode were also computed for the case $I^*(\psi) = 1-\psi$, $q_0 = 1.05$, aspect ratio of internal plasma 4.2, elongation of internal plasma 3.0. First, the ballooning marginally stable pressure profile was computed. Then $dp/d\psi$ was scaled to get n = 1 external mode stability. At marginal n = 1 stability we get $g \equiv \beta\, a\, B_0/\mu_0 I_p = 3.5$. The limiting $\beta$ -value against external n = 1 mode is barely effected by the presence of the mantle. Let us note that there are two unstable n = 1 modes with different increments even for an up-down symmetric doublet plasma corresponding to a single unstable mode in a single domain plasma. The two modes differ mainly in mode structure outside separatrix.

5. The validity of the developed codes was demonstrated with various convergence studies, checking against analytical solutions and benchmarking with other codes. Stability criteria for high-n ballooning and localized Mercier modes were implemented. Automatic pressure profile optimization against ballooning mode stability can also be performed. Preliminary studies of doublet configuration stability have shown that both n = 0 and n = 1 external modes are not more unstable than for a single plasma with nested mangetic surfaces and half the elongation. Future work should investigate doublet $\beta$-limits and n = 0 stability in more detail including the effect of up-down asymmetry.

Acknowledgement: This work was partly supported by the Swiss National Science Foundation.

References

1. F. Troyon et al., Plasma Phys. and Contr. Fusion **26** (1984) 209.
2. A. Roy and F. Troyon, 17th EPS Conf. on Contr. Fusion and Plasma Heating, Amsterdam, June 1990, **14B, Part II** (1990) 958.
3. J.C. Wesley et al., Proceedings of 8th IAEA Conf. on Plasma Physics and Contr. Fusion, Brussels 1980, **1** (1980) 35.
4. T.S. Wang, F.J. Helton, Comput. Phys. Commun. **24** (1981) 255.
5. L.M. Degtyarev, V.V. Drozdov, Computer Phys. Reports **2** (1985) 342.
6. D.E. Shumaker, J. Comput. Phys. **53** (1984) 456.
7. S. Semenzato, R. Gruber, H.P. Zehrfeld, Comput. Phys. Reports **1** (1984) 389.
8. F. Wysocki, R.C. Grimm, J. Comp. Phys. **66** (1986) 225.
9. R. Gruber, J. Comput. Phys. **26** (1978) 379.
   R. Gruber, J. Rappaz, Finite element methods in ideal linear magnetohydrodynamics. (Springer series in computational physics, Springer, 1985).
10. L.M. Degtyarev, S.Yu. Medvedev, Comput. Phys. Commun. **43** (1986) 29.
11. R. Gruber et al., Comput. Phys. Commun. **24** (1981) 363.
12. R. Gruber et al., Phys. Reports **207** (1991) 167.

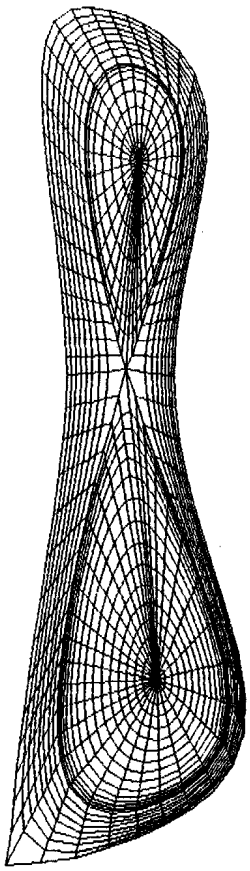

*Fig.1. Up-down asymmetric equilibrium with grid adapted to magnetic surfaces. Corresponds to the analytic solution Eq.(3).*

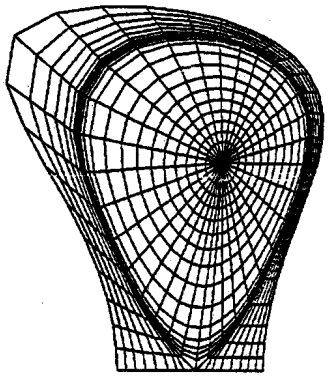

*Fig.2. Up-down symmetric equilibrium with grid adapted to magnetic surfaces. The region outside separatrix is pressureless and currentless.*

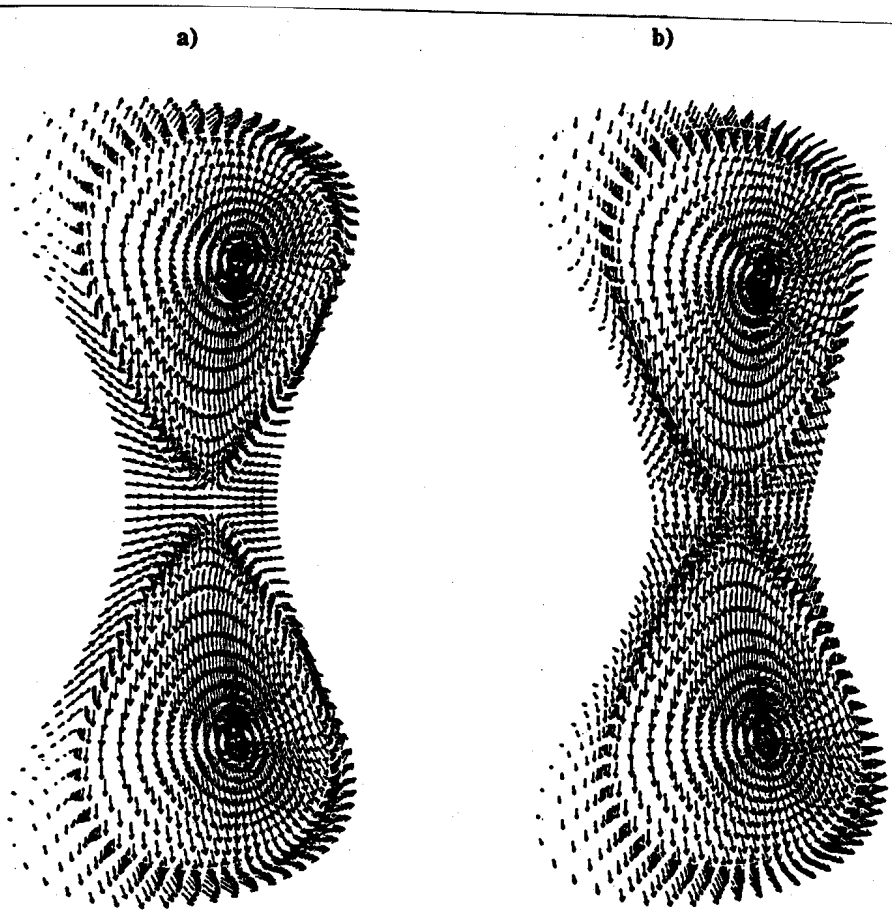


*Fig.3. Displacement fields of n=0 modes for a wall far from plasma boundary; (a) most unstable mode, $\omega^2/\omega_A{}^2 = -10^{-2}$; (b) lower growth rate mode, $\omega^2/\omega_A{}^2 = -0.5\ 10^{-2}$.*

# ELECTRON CYCLOTRON RESONANCE HEATING CALCULATIONS FOR TCV

A. Pochelon, K. Appert, T.P. Goodman, M. Henderson, A. Hirt, F. Hofmann, A. Kritz*, J.-M. Moret, R.A. Pitts, M.Q. Tran, H. Weisen and D.R. Whaley
Centre de Recherches en Physique des Plasmas, Association EURATOM - Confédération Suisse, Ecole Polytechnique Fédérale de Lausanne, 21, Av. des Bains, CH-1007 Lausanne, Switzerland
* Lehigh University, Bethlehem, Pennsylvania, U.S.A.

The TCV objective is to study the influence of elongation and strong shaping on tokamak performance. In particular, the experimental programme will concentrate on the creation and control of highly elongated plasmas ($\kappa \equiv b/a \leq 3$, $R/a=3.7$, $B=1.43T$), on the study of their operational limits and on their confinement properties.

As a consequence both of the large variety of possible plasma configurations and because of its flexibility, ECRH is the most suitable heating system for the TCV tokamak. All plasma shapes, including those with high elongation, can be heated using rotatable mirrors. In addition, the localization of the energy deposition possible with ECRH can be used for modification of the current profile (through control of the electron temperature profile) and hence for the creation of the broad current profiles necessary for vertical stability at high elongation [1]. An ECRH pulse length of 2s has been chosen so as to be of the same magnitude or greater than current diffusion times.

For the EC frequencies, the choice of extraordinary propagation modes in second X2 (83GHz) and third X3 (118GHz) harmonics permits heating at the nominal toroidal magnetic field (1.43T) in a high density plasma. With cut-off densities of 4.3 and $11.5\times10^{19}m^{-3}$ respectively, combined X2 and X3, heating at fields between 90% and 100% of the nominal value is possible at high elongation. A power of 3MW in X2 and 1.5MW in X3 is planned.

Ray-tracing calculations of the resonance accessibility from the various TCV ports with realistic beam divergence have been performed using the TORAY code [2], employing (weakly) relativistic description for both dispersion and absorption. Accounting for plasma configurations from circular to fully elongated and imposing various density profiles, these calculations lead to the selection of horizontal to oblique lateral launch for second harmonic heating and current drive and quasi-vertical top launch for X3 high density heating.

X2 heating: Wave power in X2 can reach any region of the plasma when launched from the upper lateral ports, since room for mirror adjustment permits a wide range of poloidal launch angles. The EC power is nearly 100% first-pass absorbed and can be deposited in the central region ($x \equiv r/a \leq 0.4$) if the density is below cut-off on axis. By adjusting the mirror, X2 launched from the same upper lateral ports, can efficiently be absorbed close to the plasma edge at high density (70% first-pass absorption limit at

x~0.85-0.9 in ohmically heated plasma at κ=2), making it appropriate for profile control.

The effect of refraction due to relativistic effects was analysed in detail for O1 in [3]. For X2, ray-tracing results based on both the cold plasma and the relativistic plasma approximation are compared in Fig. 1. At incidence angles very oblique to the resonance, relativistic effects profoundly modify the ray trajectory and hence the absorbed power. Refraction including relativistic effects restricts somewhat power deposition at x=0 just below cut-off density on axis, due to the reflection at the resonance. Higher $T_e$ results in more rounded trajectories with refraction being experienced earlier.

X3 heating: In contrast to X2, X3 is launched from a port at the top of the vessel giving a beam path quasi-parallel to the resonance, Fig. 2. This results in geometrically enhanced first-pass absorption [4], even for mildly elongated plasmas. Launched from the top port, X3 power results in efficient central deposition for a broad range of density. With a moderate elongation, κ=2, and density $n_{eo} \leq 7\times10^{19}$ m$^{-3}$, first-pass absorption of 60% is achieved in an ohmically heated plasma (see Fig. 3) and is more than 95% absorbed in a supplementary heated plasma ($T_e \sim 2\times T_{eOH}$). For full elongation κ=3, first-pass absorption increases to 80% and 100%, respectively. Due to the small imaginary refractive index, relativistic effects on refraction are not significant in X3 and there is no visible change of ray trajectory at the resonance.

Combination of X2-X3 heating: The accessible density ranges and corresponding radial deposition locations of X2 and X3 permit the simultaneous use of X2 and X3 gyrotrons for combined heating in plasmas with central density below $n_{eo} \sim 7\times10^{19}$ m$^{-3}$.

Maintaining n = 0 vertical stability at high elongation and low plasma current requires current profile tailoring. Off-axis heating is used to produce a local decrease of resistivity. An estimate of the power deposition profile required to obtain stable current profiles has been made assuming the Rebut-Lallia transport model. This power deposition profile is compatible with EC absorption calculations and, for a particular case at κ=2.5, vertical stability is achieved with 4MW of ECRH power.

Power loading on the walls: A simple 1D model of the scrape-off layer, together with field line tracing of various magnetic equilibria, is used to compute the total power conducted and convected to the divertor target tiles for the case of 2s ECRH pulses at the full power of 4.5MW. The calculations predict peak power densities of 1 to 7MW/m$^2$, the power deposition depending strongly on the divertor configuration (principally X-point to wall separation). Estimates of the resulting temperature rise indicate this is always below the threshold for the carbon bloom in the absence of severe tile misalignments.

TCA X1-O1 HFS heating results: The results of X1 and O1 heating at 39GHz in TCA can be used as an indication of the validity of the relativistic effects on refraction observed in X2 ray-tracing calculations. The beam in TCA was launched from a top high field side (HFS) steering mirror [5] movable in both the toroidal and poloidal directions. Thomson scattering and a soft X-ray absorber method were used to measure electron temperatures [5].

The effect of perpendicular ($\varphi=0^{\circ}$) and toroidally oblique ($\varphi=24^{\circ}$) injection on the central electron temperature in a series of TCA shots with varying density with X and O-mode HFS launch was examined. It was observed that the X-mode behaved as expected classically, with small first-pass absorption for perpendicular injection and increasing absorption with increasing toroidal angle (see Fig. 4). The same trend is obtained in (relativistic) TORAY runs, in which rays cross the resonance without refraction.

In contrast, the O-mode was not observed to behave classically. The latter implies maximum absorption for perpendicular injection and monotonically decreasing absorption for an increasing toroidal angle. This is not shown by the measurements in Fig. 4, where O($0^{\circ}$)- and O($24^{\circ}$)-results are compared. However, the experimental trend agrees with TORAY single-ray simulations, Fig. 5a, showing: **a**) a maximum in the absorption for toroidal angles $\varphi$ between $15^{\circ}$ - $30^{\circ}$ (due to geometrical absorption enhancement), **b**) an abrupt 3D "relativistic" direction change at the resonance, further increasing absorption for rays at angles between $\varphi\sim15^{\circ}$-$20^{\circ}$ (see Fig. 5b-5c) and **c**) a decrease in the absorption below the classical level (horizontal injection) for angles $\varphi<10^{\circ}$. Multiple-ray calculations are in progress to complement these single-ray results, which show that, in the case of HFS O-mode injection, relativistic effects on refraction can result in a decreased absorption for small angles and an increased absorption for medium and large angles, a general trend which appears to be confirmed by the experimental results.

Acknowledgements: This work was partially supported by the Swiss National Science Foundation.

References

[1] G. Erickson, A. Bondeson, D.J. Ward, F. Hofmann and L. Villard, Proc. EPS Conf. on Plasma Phys., Insbruck (1992)343.

[2] R.C. Myer, M. Porkolab, G.R. Smith, A.H. Kritz, Nucl. Fus. **29** (1989) 2155, and S. Yue, A. Kritz, G. Smith, 10th. Top. Conf. on Applic. of RF Power to Plasmas, Boston 1993.

[3] S. Pesic et al., 14th. IAEA Conf., Würzburg 1992, paper D4-12.

[4] R.L. Meyer et al, 7th. Top. Conf. on Applic. of RF Power to Plasmas, Kissimee, AIP Conf. Proc. **157**(1987)73.

[5] A. Pietrzyk, A. Pochelon et al., Nucl. Fus. **33**(1993)197.

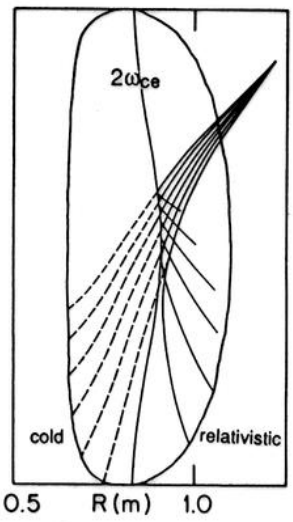


Fig. 1

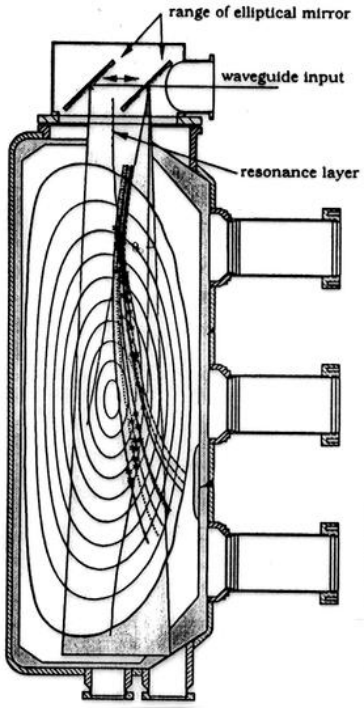


Fig. 2

Fig. 1: X2 oblique launch for cold and relativistic dispersion (1keV, $2\times10^{19}m^{-3}$). The knees at the resonance are sharper at low temperature, but disappear in the cold calculation.

Fig. 2: X3 top launch in the TCV vessel (118 GHz, $n_{eo}=7\times10^{19}\ m^{-3}$).

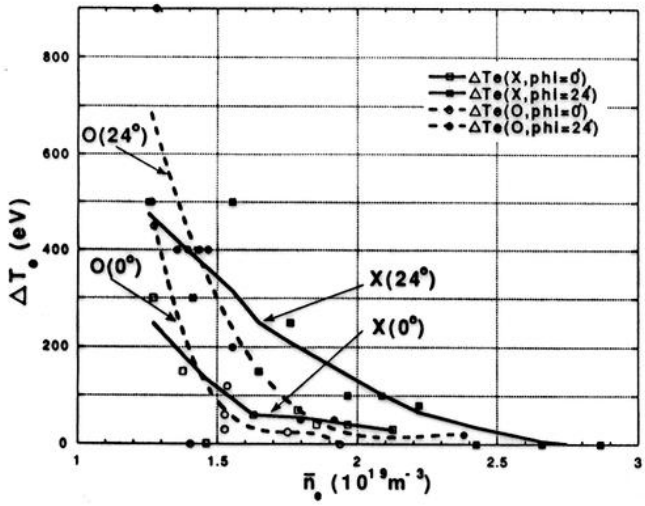


Fig. 4: Soft X-ray electron temperature increment $\Delta T_e=T_{eECRH}-T_{eOH}$ for toroidal angles $\varphi=0^o$, $24^o$, for X1 and O1 HFS launches in TCA.

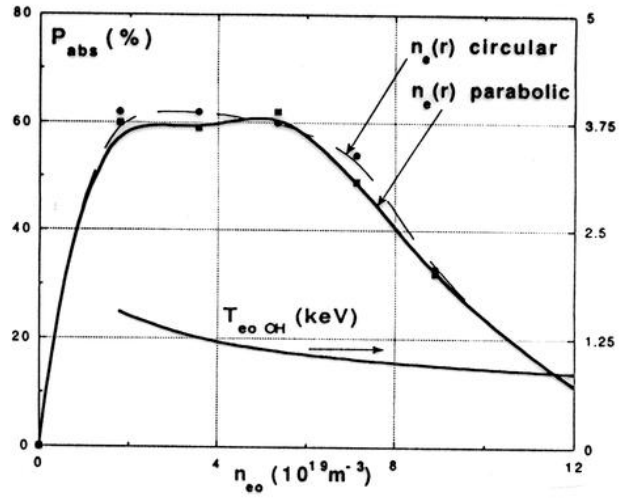


Fig. 3: First-pass absorption in X3 top launch, $\kappa=2$, ohmic temperatures, parabolic $T_e(r)$, parabolic and circular $n_e(r)$.

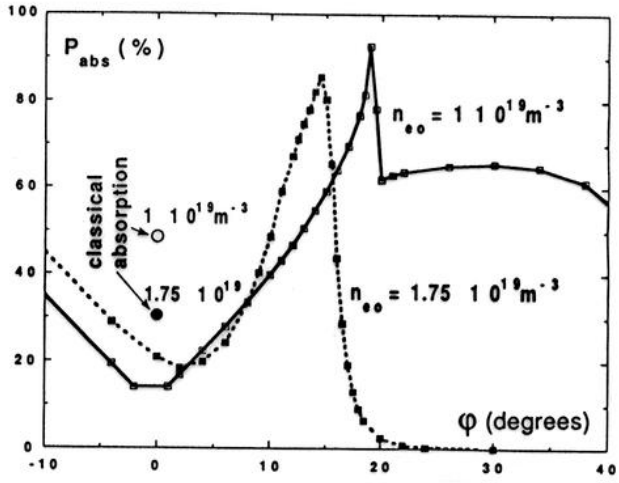


Fig. 5: a) TORAY single-ray first-pass absorption calculations for TCA O-mode cases at two densities, toroidal angle scan. Different types of refraction at the resonxance are shown in b) poloidal c) toroidal projection ($n_{eo}=1\times10^{19}m^{-3}$, $T_{eo}=1.2$keV).

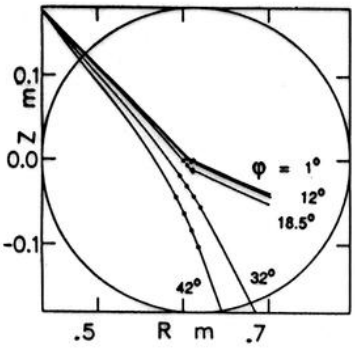


Fig. 5b)

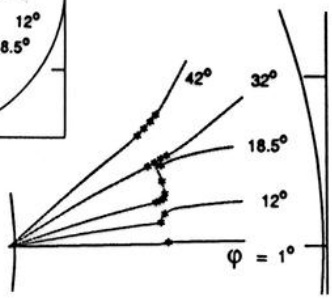


Fig. 5c)

# ALFVEN GAP MODES IN ELONGATED PLASMAS

L.Villard, J.Vaclavik, S.Brunner, H.Lütjens, and A.Bondeson

Centre de Recherches en Physique des Plasmas
Association Euratom - Confédération Suisse
Ecole Polytechnique Fédérale de Lausanne
21, av. des Bains – CH-1007 Lausanne/Switzerland

**1. Introduction.** In the context of the potential destabilization of Alfvén eigenmodes by fusion particles in tokamak reactors[1-3], it is crucial to develop a qualitative and quantitative theoretical prediction of the behaviour of these modes. Experiments are being planned at JET to excite gap modes using saddle coils. The aim of this paper is twofold. First we investigate the feasibility of gap modes excitation with saddle coils in typical JET type equilibria (single-null, up/down asymmetric configurations). Second we derive expressions for the wave-particle power transfer (in particular fast particles such as fusion alphas) that are ready to be used in global calculations of the damping/growth rates. Previous works on this type of instability[3] were theoretical analytical estimates of local growth rates.

**2. Antenna excitation of gap modes.** In order to compute ideal-MHD up/down asymmetric equilibria, modifications have been made on the CHEASE code[4]. In the actual version, plasmas with a separatrix cannot be computed and the computational boundary only approaches it. The equilibrium quantities are transferred to the global wave code LION[5]. The LION code solves the weak variational form of the wave equation with a linear finite hybrid element discretization. It computes the continuum absorption (in a non-perturbative way) and electron Landau damping due to parallel dynamics and to curvature drift in a perturbative way. The plasma is surrounded by a pure vacuum region enclosed by a perfectly conducting wall. In the vacuum region, the saddle coils are modelled by a thin current carrying sheet $D(\vec{x}) = 0$. The antenna current is written as

$$\vec{j}_a = \delta(D)\nabla D \times \nabla\alpha$$

$$\alpha(\theta,\varphi) = \sum_n \alpha_n(\theta)e^{i(n\varphi-\omega t)}, \qquad \alpha_n(\theta) = \alpha_{n0} \quad \theta_1 \le \theta \le \theta_2,$$

where $\theta_1$ and $\theta_2$ define the poloidal positions of the toroidal sections of the saddle coil and $\varphi$ is the toroidal angle. The coefficients $\alpha_{n0}$ are obtained by making the toroidal Fourier decomposition of the actual saddle coil currents. The axisymmetry of the equilibrium allows us to compute the plasma response separately for each $n$. First the solution of the wave equation and the coupled power $P_n(\omega)$ are computed with $\alpha_{n0} = 1$ for each $n$ and for various frequencies $\omega$. To obtain the coupling impedance of a particular toroidal antenna (or antenna array), we evaluate

$$R(\omega) = \frac{2}{I_a^2}\left(\sum_n I_n^2 P_n(\omega)\right),$$

where $I_n$ are the Fourier coefficients of the antenna current and $I_a$ is the total antenna current amplitude. It is planned to have up to 8 saddle coils in the JET torus. Each of the coils extends almost $\pi/2$ in the toroidal direction. With different relative phasing of these antennas, different Fourier coefficients $I_n$ are obtained. It is thus possible to select the dominant toroidal wavenumber n of the excited TAEs. An example of antenna coupling calculation is shown in Fig.1. The plasma parameters are $B_0 = 3.45T$, $R_0 = 3m$, $a = 1.05m$, $\kappa = 1.63$, $n_e = 5 \times 10^{19}m^{-3}(1 - 0.9s^2)^{0.5}$, $q_0 = 1.1$, $q_a = 3.34$, $I = 5.0MA$,

$\beta = 3.9\%$, $\beta_{pol} = 0.78$. Only the top saddle coils are activated. The dotted line in Fig.1 corresponds to the case of 2 top saddle coils at opposite toroidal locations with currents in phase opposition (+-), and the continuous line corresponds to the case of all 4 top saddle coils with currents in (+-+-) relative phasing. The 2 (+-) case excites mainly $n = 1$ modes but no $n = 2$ mode, wheras the 4 (+-+-) case excites mainly $n = 2$ modes but no $n = 1$ mode. It will therefore be possible to distinguish between TAEs having neighbouring frequencies but different $n$'s (e.g. the $n = 1$ TAE at $f = 161.7kHz$ and $n = 2$ at $f = 164.5kHz$). The JET saddle coils excite both TAEs ($f = 80 - 250kHz$) and EAEs ($f = 250 - 450kHz$). Some of the eigenmodes couple rather poorly to the saddle coil antennas. For example, let us compare the modes labelled (a) and (b) on Fig.1. These are $n = 1$ modes. Fig.2. shows their respective eigenmode wavefield structures. The mode (a) has a rather large $m = 1$ component from the magnetic axis up to the $q = 1.5$ surface where it has strong gradients. The mode (b) has a more global structure and a comparatively larger amplitude near the edge. The mode (b) has the same phase from the magnetic axis to the outer (low lield side) edge wheras the mode (a) has a change of phase near the $q = 1.5$ surface. The two types of modes are also seen for $n = 2$ and were also seen in circular plasmas[5]. Which mode is the most easily destabilized by fast particles is a question that will need careful further studies. The "internal"-like mode (a) is probably more sensitive to the fast particles in the center, whereas the "external"-like mode (b), if destabilized, could be more effective in expelling fast particles from the center to the outside. The damping of these modes will probably be affected in a different way by the different parameters. The "internal" mode may be more ion-Landau damped for sufficiently high $T_i$ plasmas, wheras the "external" mode may be more sensitive to electron-Landau damping for cases where $v_A \simeq v_{the}$ in the outer region.

**3. Damping and growth rates.** To evaluate the growth rates $\gamma$ of the waves calculated by the LION code, it is necessary to establish a relation between the total time-averaged power $\bar{P}$ absorbed by hot species and the given EM fields $(\vec{E}, \tilde{\vec{B}})$: $\gamma = -\bar{P}/2W$, where $W$ is the total energy of the wave. Working in the Alfvén frequency range, it is convenient to describe the evolution of the species using the drift kinetic equation (DKE). The equilibrium distribution functions of the guiding centers for electrons and ions are taken as local Maxwellians (functions of $\psi$ = poloidal flux). The $\alpha$-particles are described by a slowing-down distribution[6]:

$$F = N(\psi)\frac{C(\psi)}{v^3 + v_c^3(\psi)}H(v_0 - v),$$

where H is the Heaviside function and $v_0$ the birth velocity of the alphas.The fluctuating distribution function is then evaluated for given EM fields from the linearized DKE using a perturbation method. The parameter $b_p = B_p/|\vec{B}_0|$, where $B_p$ is the poloidal component of the magnetostatic field, and the parameter $|\vec{v}_d|/\lambda_\perp\omega$, where $\vec{v}_d$ is the magnetic curvature drift, $\lambda_\perp$ the wavelength perpendicular to $\vec{B}_0$ and $\omega$ the frequency of the EM fields, are considered small. Integrating the resulting distribution function over the guiding center phase space, one can evaluate the total time-averaged power exchanged between the particles and the EM fields[7]. As the EM fields are provided by an ideal-MHD calculation, the component of $\vec{E}$ parallel to the magnetostatic field is zero and must therefore be obtained from a more general model. This can be done using the quasi-neutrality condition for electrons and ions. For the electrons and ions, we obtain:

$$\bar{P} = \sqrt{\pi}\epsilon_0 \int d^3x \frac{\omega_p^2 v_{th}}{4\Omega^2|k_\parallel|} \exp -z_0^2 \times \left( |a_{species}|^2 + \left| \vec{\beta}_\perp \cdot \vec{E} - i\omega \tilde{B}_\parallel \right|^2 \right),$$

$$
\begin{aligned}
a_{electron} &= \frac{1}{1-Z}\left(i\frac{\omega}{\Omega_i}\nabla\cdot\vec{E}_\perp + \vec{\beta}_\perp\cdot\vec{E}_\perp\right), \\
a_{ion} &= \frac{T_e}{T_i}\frac{1}{1-Z}\left(i\frac{\omega}{\Omega_i}\nabla\cdot\vec{E}_\perp + \vec{\beta}_\perp\cdot\vec{E}_\perp\right) - i\omega\left(1+\frac{T_e}{T_i}\right)\tilde{B}_{||} \\
&\quad + \left[1+\frac{T_e}{T_i}+2\left(\frac{\omega}{k_{||}v_{thi}}\right)^2\right]\vec{\beta}_\perp\cdot\vec{E}_\perp,
\end{aligned}
$$

where $\omega_p$ is the plasma frequency, $\Omega$ the cyclotron frequency, $k_{||}$ the parallel wave number, $z_0 = \omega/k_{||}v_{th}$, $\vec{\beta}_\perp = \left(\nabla\times\vec{e}_{||0}\right)_\perp$, $\vec{e}_{||0} = \vec{B}_0/B_0$ and $Z = Z(\omega/|k_{||}|v_{the})$ the dispersion function. For the $\alpha$-particles we also consider the contributions due to the inhomogeneities of equilibrium:

$$
\begin{aligned}
\vec{P}^{\alpha}_{homo} &= \pi^2\epsilon_0\int d^3x\frac{\omega_{p\alpha}^2 C}{|k_{||}|\Omega_\alpha^2}\left\{\left[\frac{v_p^4}{|v_p|^3+v_c^3}+2v_p^2 I_0\right]\left|\vec{\beta}_\perp\cdot\vec{E}\right|^2\right. \\
&\quad \left. +2\omega v_p^2 I_0\Im m\left(\tilde{B}_{||}\vec{\beta}_\perp\cdot\vec{E}^*\right)+I_1\left|\vec{\beta}_\perp\cdot\vec{E}-i\omega\,\tilde{B}_{||}\right|^2\right\}, \\
\vec{P}^{\alpha}_{inhomo} &= \frac{\pi^2\epsilon_0}{\omega}\Im m\int d^3x\nabla'\frac{\omega_{p\alpha}^2 C}{|k_{||}|\Omega_\alpha^3}\left\{\left(v_p^4 I_0+v_p^2\frac{I_1}{2}\right)\vec{\beta}_\perp\cdot\vec{E}\right. \\
&\quad \left. +\left(v_p^2\frac{I_1}{2}+\frac{I_2}{4}\right)\left(\vec{\beta}_\perp\cdot\vec{E}-i\omega\,\tilde{B}_{||}\right)\right\}(\vec{\beta}_\perp\cdot\nabla)E_b^*,
\end{aligned}
$$

$$
\text{where}\quad I_n = \int_{|v_p|}^{v_0} dv\frac{v\left(v^2-v_p^2\right)^n}{v^3+v_c^3}
$$

and $\nabla'$ is equivalent to $|\nabla\psi|\partial/\partial\psi$ except that it operates only on density and temperature.

**4. Conclusion.** It was shown that saddle coils can be used to excite low $n$ TAEs and EAEs in typical single-null JET plasmas. Toroidal mode number selection can be done by different phasings of the antennas. Some of the eigenmodes couple weakly but may be important to study. In the future, the expressions developed for global growth and damping rates will be used in the global calculation of gap modes.

**Acknowledgements.**
One of the authors (L.V.) wishes to thank Drs A.Fasoli, G.Huysmans, J.Jacquinot, J.B.Lister and W.Kerner for interesting discussions. This work was partly supported by the Swiss National Science Foundation.

**References.**

[1] K.L.Wong et al., Phys.Rev.Lett. **66** (1991) 1874.
[2] W.W.Heidbrink et al., Nucl.Fus. **31** (1991) 1635.
[3] G.Y.Fu, C.Z.Cheng, Phys.Fluids B**4** (1992) 3722.
[4] H.Lütjens, A.Bondeson, A.Roy, Comput.Phys.Commun. **69** (1992) 287.
[5] L.Villard, G.Y.Fu, Nucl.Fus. **32** (1992) 1695.
[6] R.Koch, Phys.Lett. A **157**, (1991) 399.
[7] S.Brunner and J.Vaclavik, On Absorption of Low Frequency Electromagnetic Fields, LRP 471/93, CRPP, Lausanne (1993).

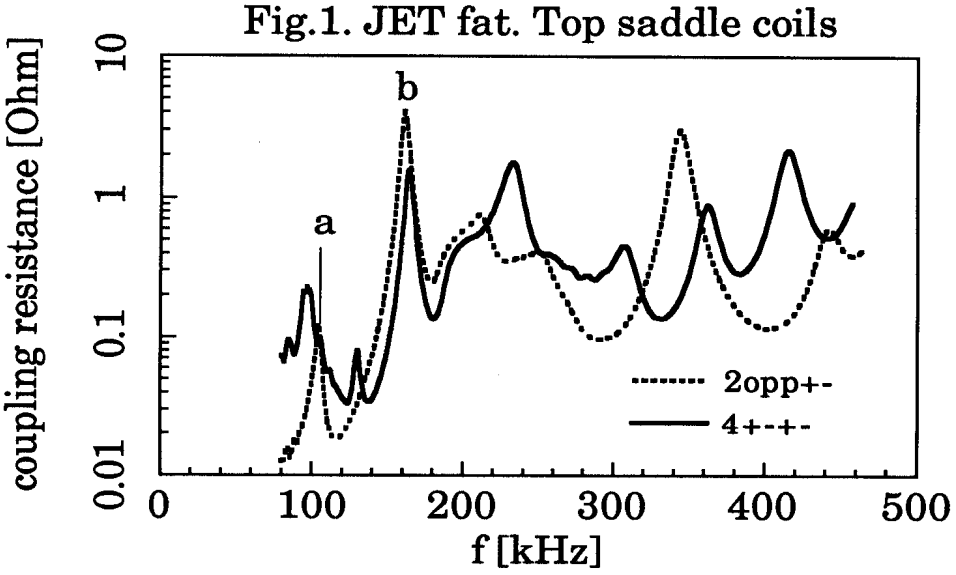


*Fig.1. Coupling resistance of saddle coils . 2 antennas with opposite phasings (dotted line), 4 antennas with (+-+-) phasings (continuous line). Up-down asymmetric JET equilibrium with $R/a=2.77$, $\kappa=1.63$, $q_0=1.1$, $q_a=3.34$, $\beta=3.9\%$, $\beta_{pol}=0.78$, $B_0=3.45T$, $I_p=5.0MA$, $n_e=5.10^{19}(1-0.9s^2)^{1/2}\ m^{-3}$.*

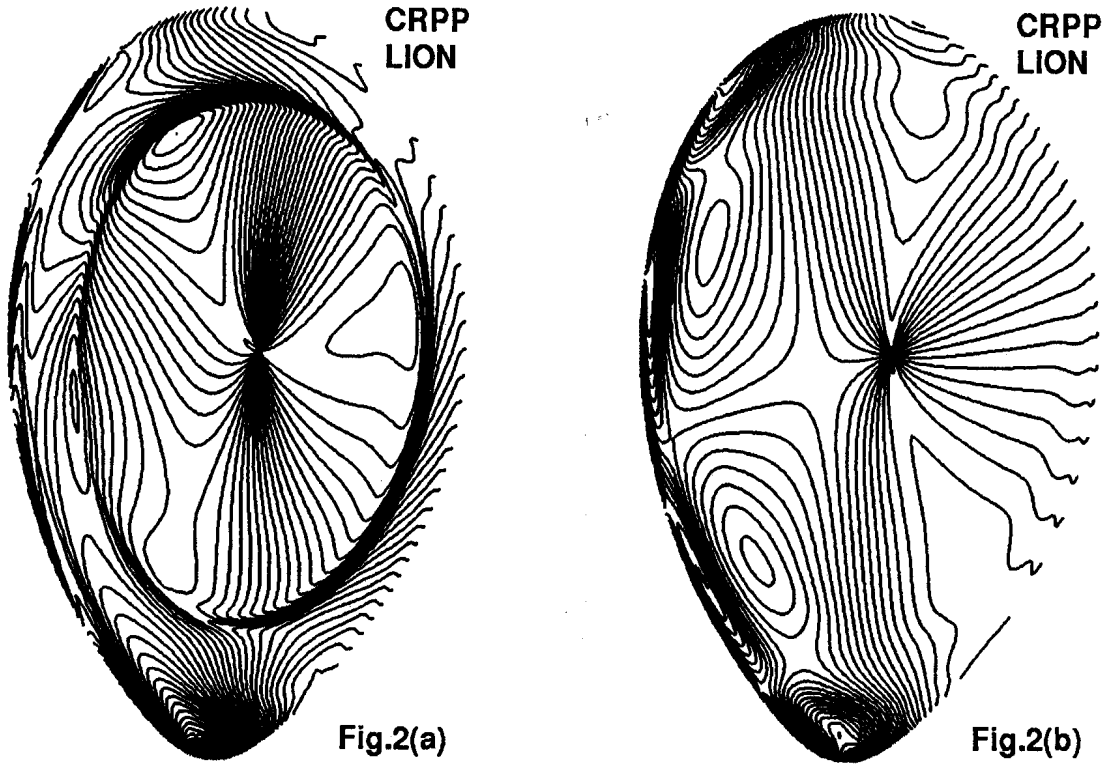


*Fig.2. Level line plots of n=1 TAEs $Re(E_b)$ wavefields (radial displacement) for the cases (a) and (b) corresponding to Fig.1.*

# Pressure and Inductance Effects on the Vertical Stability of Shaped Tokamaks

D. J. Ward, A. Bondeson, F. Hofmann,
Centre de Recherches en Physique des Plasmas,
Association Euratom–Confédération Suisse, EPFL, Lausanne

In previous work [1] it was shown that the combination of triangularity and high $\beta_p$ is strongly stabilizing for axisymmetric modes in highly elongated ($2.5 < \kappa < 3.0$) tokamak plasmas. The effect of pressure in dee shaped plasmas reduces the driving energy of the instability. In contrast, in an inverse-dee pressure is highly destabilizing. In a pure ellipse pressure has a negligible effect on the free space growth rate, but is somewhat stabilizing in the presence of a resistive or ideal wall. The purpose of the present note is to extend the study of shape and profile effects to cross-sections of moderate elongation in the range $1.6 \leq \kappa \leq 2$.

The primary results from Ref. [1] are shown in Fig. 1. Here an upper limit on the growth rate of the vertical instability is specified (such an upper limit is imposed by limitations of the active feedback system), and we find that the stability boundary in terms of the operational parameters $l_i$ and $\beta_p$ is very nearly linear. This boundary defines a region of stability (toward low $l_i$ and high $\beta_p$) for a given shape of the plasma cross section. This stability boundary is nearly independent of the details of the current profile, and also independent of the aspect ratio if the boundary is plotted in terms of $l_i$ vs. $\epsilon\beta_p$. We see from Fig. 1 that the slope of this boundary increases strongly with increasing triangularity, and decreases with increasing elongation.

Here we present some first results from a comprehensive study of the effects of triangularity, pressure, and profile effects in moderately shaped ($\kappa = 1.6$–$2.0$) tokamak plasmas surrounded by a resistive wall. These results again show the stabilizing effect of triangularity and pressure.

The resistive wall stability calculations are performed using the NOVA-W [2] stability code with equilibria calculated using the CHEASE equilibrium code [3]. For the cases shown in Figs. 2 & 3, the resistive wall is specified to be conformal to the plasma shape, and to be at a distance from the plasma at the midplane of 1.4 times the plasma minor radius, $d = 1.4a$. The resistive wall has a ratio of resistivity to wall thickness of $\eta/\delta_w = 4 \times 10^{-5}\Omega$.

The plasma–vacuum boundary is specified as

$$R/a = A + \cos(\theta + \delta \sin\theta + \lambda \sin 2\theta) \quad , \quad Z/a = \kappa \sin\theta \tag{1}$$

where $\kappa$ is the elongation, $\delta$ is the triangularity, and $\lambda$ is a squareness parameter (used in some of the cases shown in Fig. 1). The following definitions are used for the poloidal beta, $\beta_p \equiv (4/\mu_0 I_p^2 R_0) \int_{pl} p\, d^3x$, and internal inductance, $l_i \equiv (2/\mu_0^2 I_p^2 R_0) \int_{pl} B_p^2\, d^3x$.

Figure 2 shows results for equilibria with elongation $\kappa = 1.8$ for several different values of triangularity ranging from $\delta = 0$ to $\delta = 0.5$. The resistive wall growth rate $\gamma$ (in $s^{-1}$) is plotted vs. $\beta_p$. For each value of triangularity two pressure profile specifications are used: one peaked, with pressure peaking factors $PPF \approx 3.3$, and one relatively flat, with $PPF \approx 2$. The same current profile is specified for all cases in this figure yielding $l_i \approx 0.75$.

Figure 2 shows the stabilizing effect of high $\beta_p$ in all cases except for the pure ellipse with a peaked pressure profile. This stabilizing effect increases strongly with triangularity. Only at very low values of $\beta_p$ do the high-triangularity equilibria have higher

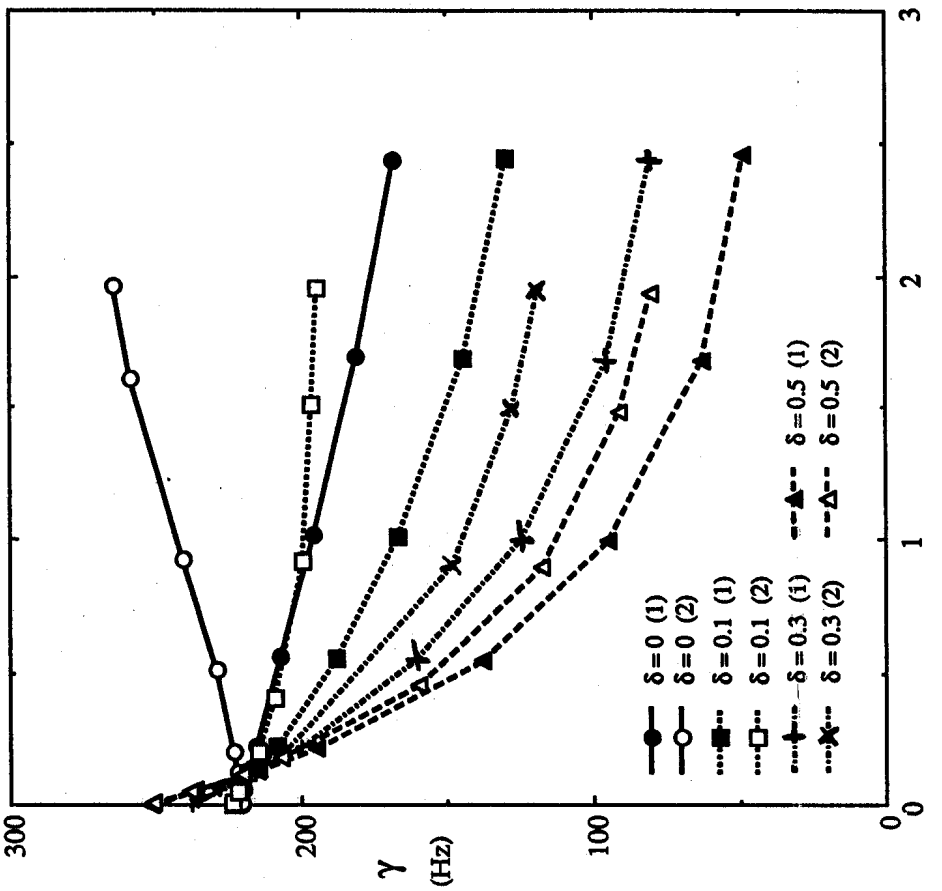


Figure 2

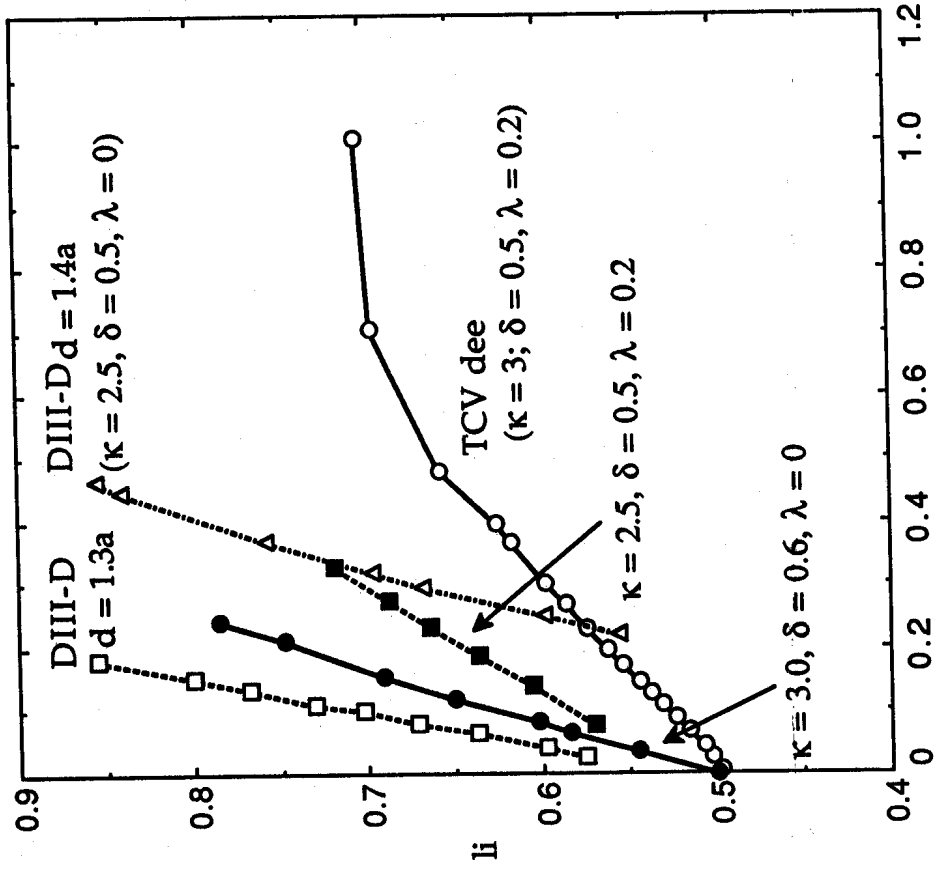


Figure 1

growth rates than those at lower triangularity. Here, at $\beta_p = 0$, the $\delta = 0.5$ equilibria have growth rates higher than those at $\delta = 0$ by about 15%. Furthermore, the shape of the pressure profile has only a modest influence on the stability. The stabilization by pressure and positive triangularity is somewhat stronger for the broader pressure profiles.

Figure 3 shows results for the same shapes and wall but with a narrower current profile, so that $l_i \approx 0.95$. Here, the growth rates are higher than in Fig. 2 (note the difference in the scale) owing to the reduced coupling of the current profile to the wall. For the low-triangularity cases there is a much larger increase in the growth rates as the inductance is increased than for the high-triangularity cases. In fact, the growth rates at $\beta_p = 0$ for the $\delta = 0$ equilibria almost double in magnitude as $l_i$ is increased from $l_i \approx 0.75$ to $l_i \approx 0.95$, whereas the growth rates for the $\delta = 0.5$ equilibria increase by only about 20%. Note that for this high-inductance current profile, the higher-triangularity cases are more stable than the low-triangularity cases for all values of $\beta_p$.

We find that the results for cases with higher elongation ($\kappa = 2$) give the same trends, but naturally with higher growth rates. One clear conclusion is that with any nonzero triangularity the most unstable equilibria are those with $\beta_p = 0$. Therefore, low-pressure operation gives the most restrictive conditions on the vertical stability for a given configuration. We consider now these zero-pressure cases and the variation of growth rate with respect to the resistive wall distance.

Figure 4 shows how the growth rate varies with respect to the normalized distance $d/a$ of the resistive wall for various values of triangularity and with $\beta_p = 0$. We see that for the cases with the broader current profiles ($l_i \approx 0.75$) the growth rates for equilibria with different triangularities are quite similar, with the high-triangularity cases being slightly more unstable. However, equilibria with narrower current profiles ($l_i \approx 0.95$) show a much greater variation in growth rate with respect to the amount of triangularity, and the high-triangularity cases are more stable. In fact, the curves for $\delta = 0.5$ are fairly close in magnitude for the broad and narrow current profiles, as mentioned above. The curves are shown for both the $\kappa = 1.8$ and the $\kappa = 2$ equilibria. At zero triangularity the $\kappa = 1.8$ equilibria with $l_i \approx 0.95$ have growth rates quite close to those of the $\kappa = 2$ equilibria with $l_i \approx 0.71$, whereas at triangularity $\delta = 0.5$ the growth rates for the $\kappa = 1.8$ cases remain well below those for the $\kappa = 2$ cases for the broad and narrow current profiles.

## CONCLUSION

The combination of high triangularity and high $\beta_p$ is strongly stabilizing for the vertical instability in tokamak plasmas surrounded by a resistive wall. For narrow current profiles triangularity is stabilizing even at $\beta_p = 0$. Only with broader current profiles at very low values of $\beta_p$ do the high-triangularity cases have larger growth rates than the low-triangularity cases (and only by about 10–15% at zero pressure). Also, the variation in resistive wall growth rate with respect to changes in the internal inductance is much smaller at high triangularity. We conclude, therefore, that high triangularity is generally beneficial for vertical stability in elongated tokamak plasmas.

[1] D. J. Ward, A. Bondeson, and F. Hofmann, LRP 468/92, CRPP-EPFL, Lausanne (December 1992). To appear in Nucl. Fusion **33** (1993) #5 or #6.

[2] D. J. Ward, S. C. Jardin, and C. Z. Cheng, J. Comput. Phys. **104** (1993) 221.

[3] H. Lütjens, A. Bondeson, and A. Roy, Comput. Phys. Commun. **69** (1992) 287.

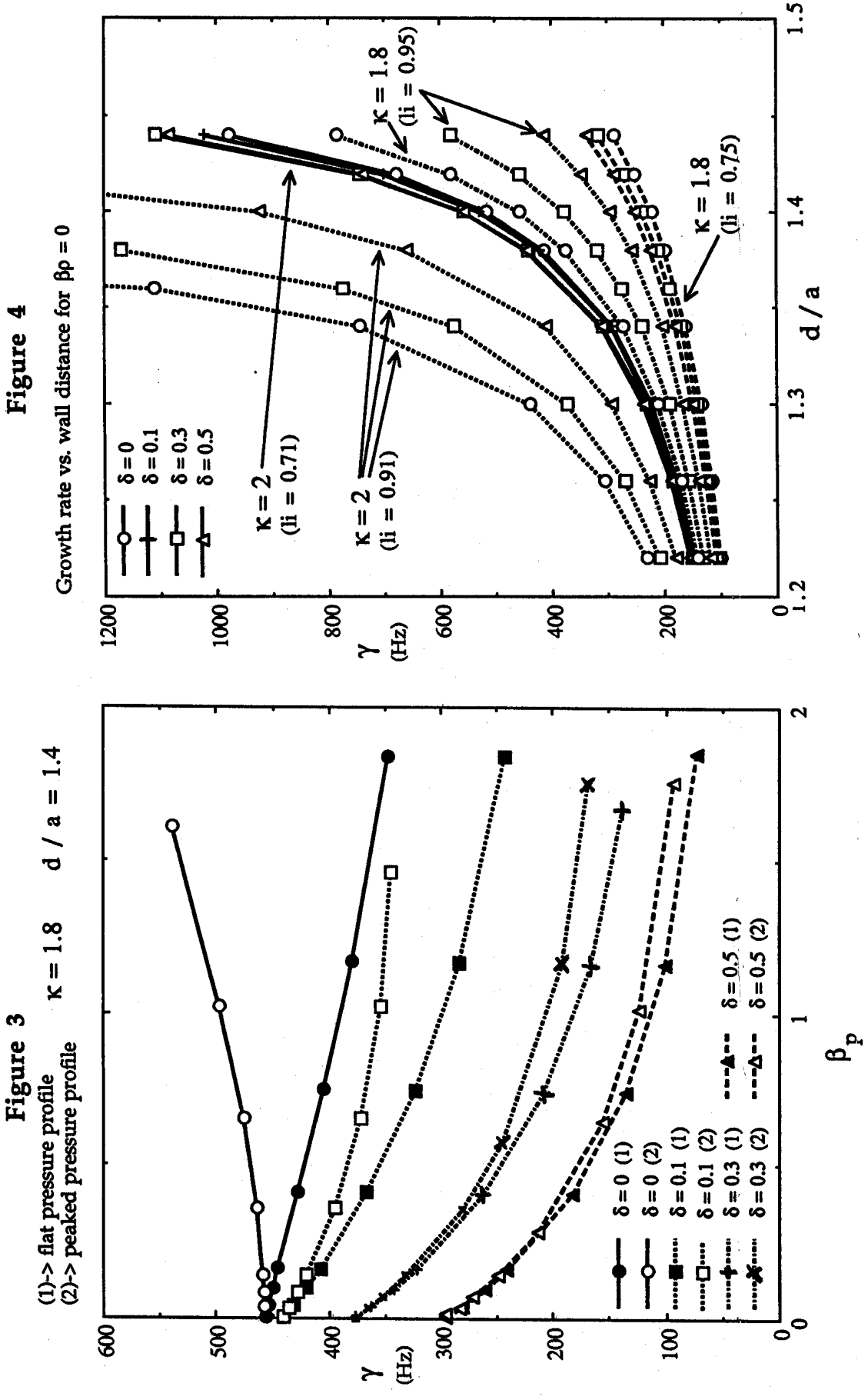
Figure 3
(1)-> flat pressure profile
(2)-> peaked pressure profile
κ = 1.8 d / a = 1.4
γ (Hz)
β_p
δ = 0 (1)
δ = 0 (2)
δ = 0.1 (1)
δ = 0.1 (2)
δ = 0.3 (1)
δ = 0.3 (2)
δ = 0.5 (1)
δ = 0.5 (2)
Figure 4
Growth rate vs. wall distance for βp = 0
γ (Hz)
d / a
δ = 0
δ = 0.1
δ = 0.3
δ = 0.5
κ = 2 (li = 0.71)
κ = 2 (li = 0.91)
κ = 1.8 (li = 0.95)
κ = 1.8 (li = 0.75)